

This is an Open Access document downloaded from ORCA, Cardiff University's institutional repository:<https://orca.cardiff.ac.uk/id/eprint/120066/>

This is the author's version of a work that was submitted to / accepted for publication.

Citation for final published version:

Ren, Dingkun, Azizur-Rahman, Khalifa , Rong, Zixuan, Juang, Bor-Chau, Somasundaram, Siddharth, Shahili, Mohammad, Farrell, Alan C., Williams, Benjamin S. and Huffaker, Diana L. 2019. Room-temperature midwavelength infrared InAsSb nanowire photodetector arrays with Al<sub>2</sub>O<sub>3</sub> passivation. *Nano Letters* 19 (5) , pp. 2793-2802. 10.1021/acs.nanolett.8b04420

Publishers page: <http://dx.doi.org/10.1021/acs.nanolett.8b04420>

Please note:

Changes made as a result of publishing processes such as copy-editing, formatting and page numbers may not be reflected in this version. For the definitive version of this publication, please refer to the published source. You are advised to consult the publisher's version if you wish to cite this paper.

This version is being made available in accordance with publisher policies. See <http://orca.cf.ac.uk/policies.html> for usage policies. Copyright and moral rights for publications made available in ORCA are retained by the copyright holders.



# Room-Temperature Mid-Wavelength Infrared InAsSb Nanowire Photodetector Arrays with Al<sub>2</sub>O<sub>3</sub> Passivation

*Dingkun Ren,<sup>\*†</sup> Khalifa M. Azizur-Rahman,<sup>‡</sup> Zixuan Rong,<sup>†</sup> Bor-Chau Juang,<sup>†</sup> Siddharth  
Somasundaram,<sup>†</sup> Mohammad Shahili,<sup>†</sup> Alan C. Farrell,<sup>†</sup> Benjamin S. Williams,<sup>†#</sup> and  
Diana L. Huffaker<sup>†‡#</sup>*

<sup>†</sup> Department of Electrical and Computer Engineering, University of California, Los Angeles, Los Angeles, California 90095, United States

<sup>‡</sup> School of Physics and Astronomy, Cardiff University, Cardiff, Wales CF24 3AA, United Kingdom

<sup>#</sup> California NanoSystems Institute, University of California, Los Angeles, Los Angeles, California 90095, United States

## **ABSTRACT**

Developing uncooled photodetectors at mid-wavelength infrared (MWIR) is critical for various applications including remote sensing, heat seeking, spectroscopy, and more. In this study, we demonstrate room-temperature operation of nanowire-based photodetectors at MWIR composed of vertical selective-area InAsSb nanowire photoabsorber arrays on large bandgap InP substrate with nanoscale plasmonic gratings. We accomplish this by significantly suppressing the nonradiative recombination at the InAsSb nanowire surfaces by introducing *ex-situ* conformal Al<sub>2</sub>O<sub>3</sub> passivation shells. Transient simulations estimate an extremely low surface recombination velocity on the order of 10<sup>3</sup> cm/s. We further achieve room-temperature photoluminescence emission from InAsSb nanowires, spanning the entire MWIR regime from 3 μm to 5 μm. A dry-etching process is developed to expose only the top nanowire facets for metal contacts, with the sidewalls conformally covered by Al<sub>2</sub>O<sub>3</sub> shells, allowing for a higher internal quantum efficiency. Based on these techniques, we fabricate nanowire photodetectors with an optimized pitch and diameter and demonstrate room-temperature spectral response with MWIR detection signatures up to 3.4 μm. The results of this work indicate that uncooled focal plane arrays at MWIR on low-cost InP substrates can be designed with nanostructured absorbers for highly compact and fully integrated detection platforms.

## **KEYWORDS**

Nanowire, MWIR, photodetector, uncooled, InAsSb, Al<sub>2</sub>O<sub>3</sub>, passivation

III-V semiconductor photodetectors operating at mid-wavelength infrared (MWIR, 3 – 5  $\mu\text{m}$ ) are the sensors of choice for the most demanding applications including heat seeking, remote sensing, gas monitoring, deep-space imaging, and spectroscopy. Various types of MWIR cameras are commercially available and show outstanding detectivity. Most of them are based on InSb,<sup>1,2</sup> mercury cadmium telluride (MCT),<sup>2</sup> or InAs-GaSb type-II superlattice focal plane arrays (FPAs);<sup>4</sup> however, they all require additional cooling accessories to achieve high signal-to-noise ratio. Additionally, these detectors also offer multispectral/hyperspectral capability spanning the MWIR. To achieve this, a combination of the following approaches has been implemented: (1) additional optical equipment (including filter wheels) that disperse light to different FPA, (2) vertical stacks of detectors that have different spectral sensitivities,<sup>5,6</sup> and (3) tunable Fabry-Perot (F-P) cavity filter atop FPAs (also referred to as adaptive focal plane arrays – AFPA).<sup>5,7</sup> Unfortunately, all of these approaches increase device complexity. Hence, significant research interest has been generated to develop high-sensitivity and high-resolution uncooled photodetectors with efficient multispectral/hyperspectral capability in MWIR wavelength regime.

Bottom-up vertical III-V semiconductor nanowire-material systems provide significant promise for MWIR multispectral detector application due to their unique optoelectronic properties. Their extremely small fill factor (<5%) allows for a significant reduction of absorption volume and dark current.<sup>8</sup> Plasmonic structures can be further integrated with nanowires to increase absorption in the small nanowire volume and offer tunable absorption across the MWIR spectrum by varying the array geometrical parameters. Thus nanowire-plasmonic structures can be efficiently utilized for multispectral/hyperspectral applications without the need for additional device features.<sup>9</sup> Additionally, nanowires can also be heteroepitaxially grown on large bandgap substrates (e.g. Si, GaAs or InP) with high-quality heterointerfaces, offering unique opportunities for suppressing minority carrier diffusion and enabling hybrid integration.<sup>8,10-16</sup> This is because threading dislocations and point dislocations can be minimized by elastic deformation at the nanowire-substrate heterointerfaces, a prospect infeasible in thin-film epitaxy. Great progress has been made recently on InAsSb-based nanowire devices towards achieving photodetection at MWIR. This ternary material spans the entire MWIR regime due to its tuneable energy bandgap. Examples of some pioneering

works include (1) *n*-InAsSb nanowires on *p*-InAs giving photoresponse up to 3.5  $\mu\text{m}$  (227 K);<sup>17</sup> (2) InAsSb *p-i-n* nanowires on *p*-Si showing a photodetection signature up to  $\sim 3$   $\mu\text{m}$  (300 K);<sup>18</sup> (3) unintentionally doped InAsSb nanowires on *n*-InAs offering spectral response between 3 – 5  $\mu\text{m}$  (5 K).<sup>19</sup> However, to the best of our knowledge no uncooled nanowire detector has been reported to show clear photodetection signatures over 3  $\mu\text{m}$ . Many studies have also shown growth of high-quality InAsSb nanowires with different antimony compositions.<sup>10-16,20-27</sup> However, improving their optical properties remains a challenge, as there have been no reported room-temperature photoluminescence (PL) emission from these nanowires spanning the entire MWIR regime. This is mainly due to the significant nonradiative recombination at the arsenic-rich InAsSb nanowire surfaces, which is well known. Since the performance of nanowire-based devices is predominantly affected by the surface quality due to their large surface-to-volume ratios,<sup>28,29</sup> it is critical to develop a high-quality surface passivation to improve the internal quantum efficiency (IQE) of InAsSb nanowire photodetectors for room-temperature photodetection at MWIR.<sup>8,9</sup>

In this work, we demonstrated uncooled InAsSb photodetector arrays on InP substrates for photodetection at MWIR, grown by selective-area metal-organic chemical vapor deposition (SA-MOCVD). We first developed the surface passivation for InAsSb nanowires using conformal Al<sub>2</sub>O<sub>3</sub> layers by atomic-layer deposition (ALD). Note that the nanowires were grown on patterns that are geometrically optimized for photodetection at MWIR. A 10- to 50-fold increase in the PL emission intensity from InAsSb nanowire arrays was observed at 77 K by introducing a sulfurized surface with Al<sub>2</sub>O<sub>3</sub> passivation layer. An extremely low surface recombination velocity on the order of 10<sup>3</sup> cm/s was estimated by three-dimensional (3-D) transient simulations of the PL process. Furthermore, room-temperature emission from InAsSb nanowire arrays was achieved, spanning the entire MWIR regime from 3  $\mu\text{m}$  to 5  $\mu\text{m}$ . We also designed a dry etching process to etch the Al<sub>2</sub>O<sub>3</sub> shell at the top of the nanowire, while keeping the sidewalls passivated, to expose only the nanowire top facets for metal contacts. No degradation of nanowire surface quality was observed after dry etching, indicating its compatibility with standard nanowire fabrication process. We finally showed the optoelectronic characterization results of fabricated InAsSb photodetector arrays, including device reflectance and room-temperature spectral response with MWIR detection signatures at 3.4  $\mu\text{m}$ . We

believe our study builds a foundation that generates further theoretical and experimental studies towards high-performance InAsSb nanowire photodetectors at MWIR. Furthermore, our work paves the way toward realizing nanowire-based uncooled multispectral/hyperspectral focal plane arrays at MWIR on low-cost substrates for highly compact and fully integrated detection platforms.

**Nanowire epitaxy.** The InAsSb nanowire array was grown on an InP (111)B substrate. The diameter and pitch (spacing) of the nanoholes were designed as 40 nm and 1300 nm, respectively. The 3-D self-aligned plasmonic gratings were used to strongly couple incident light into the nanowire top segments on plasmonic resonance (shown in the later discussion for device fabrication).<sup>17,30,31</sup> The nanowire array pitch was further set to 1300 nm to achieve plasmonic resonance in the MWIR regime.<sup>32</sup> The size of the nanowire array was  $200 \times 200 \mu\text{m}^2$ , containing a total of approximately 23,716 nanowires. Trimethylindium (TMIn), tertiarybutylarsine (TBAs), and trisdimethylaminoantimony (TDMASb) precursors were used for nanowire growth in MOCVD. We used seeding layer assisted and pulsed-arsenic growth techniques developed in our previous studies to achieve high vertical yield of  $\text{InAs}_{1-x}\text{Sb}_x$  ( $x = 0.05$ ) nanowires on a lattice mismatched InP substrate (3.2 – 3.5 % lattice mismatch).<sup>10,23</sup> The growth temperature of the nanowires was between 500 to 530°C. A thin InAs seeding layer (V/III ratio of 32) was first introduced, followed by the growth of InAsSb nanowires with V/III ratio of 2. No *in-situ* passivation layer was grown. We note that the growth of InAsSb nanowires on a nanohole pattern with large pitch (1300 nm in this case) is extremely difficult. This is because the low vapor pressure of antimony can easily lead to condensation of antimony on the nanowire sidewall or on the substrate if the growth conditions are not carefully controlled.<sup>20</sup> We found that a V/III ratio of 2 achieved the desired high vertical yield and effective antimony incorporation. A V/III ratio lower than 2 led to a lower vertical growth rate and more lateral overgrowth, while a V/III ratio higher than 2 resulted in lower antimony incorporation and excess antimony adatoms. Thus, there is a clear restriction on the usable range of V/III ratios for the growth of InAsSb nanowires. Furthermore, as the nanowire pitch was increased to 1300 nm, each nanohole shared more antimony adatoms that diffuse from the substrate. This led to an increase of the effective flow ( $[\text{TDMASb}]_{\text{eff}}$ ) and partial pressure ( $[p_{\text{Sb}}]$ ). Since it is critical to keep a low  $[p_{\text{Sb}}]$  to avoid condensation while using a low  $[p_{\text{As}}]$  to increase antimony vapor phase

concentration for high antimony solid phase composition  $[x]_{\text{Sb}}$ , the only approach is to maintain low flow rates for both precursors. However, we were limited by the mass flow controllers (MFCs) in our MOCVD system. More details of growth calibrations are discussed in the Supporting Information (Figure S1).

**Surface passivation with  $\text{Al}_2\text{O}_3$ .** To achieve uncooled nanowire photodetectors at MWIR, it is critical to develop a robust and controllable passivation technique to significantly reduce nonradiative recombination at the InAsSb nanowire sidewalls. To the best of our knowledge, to date there has been no report showing room-temperature optical signatures from InAsSb nanowires spanning the entire MWIR spectrum (3 – 5  $\mu\text{m}$ ) due to poor surface passivation. Here, we developed an *ex-situ* passivation technique based on  $\text{Al}_2\text{O}_3$  thin films by ALD. The *ex-situ* passivation is more desirable for InAsSb nanowire material system over *in-situ* passivation. First, the only lattice matched materials to arsenic-rich InAsSb are based on GaSb and AlSb; however, neither of them offers sufficient valance band offset for hole carriers. Second, although the In(As)P shells can be used as passivation layers, the large lattice mismatch would lead to increased surface leakage current due to Shockley-Read-Hall (SRH) nonradiative generation-recombination (G-R) processes and the surface strain would bend the nanowires. Conversely, the *ex-situ* passivation technique is more reliable because the thickness of passivation layer can be freely controlled by the deposition time in ALD. In addition, the etching selectivity of oxides to III-V compound semiconductors is high, and thus oxides on the nanowire tips can be selectively etched for metal contacting while nanowire sidewalls are left fully covered (shown later in the device fabrication). Thus, *ex-situ*  $\text{Al}_2\text{O}_3$  passivation is more desirable for the InAsSb nanowire material system.

The *ex-situ* passivation process was carefully designed. The samples with as-grown InAsSb nanowire arrays were submerged in a  $(\text{NH}_4)_2\text{S}$  solution for 5 minutes, i.e., sulfuration. The dilution ratio was  $(\text{NH}_4)_2\text{S}:\text{H}_2\text{O} = 1:10$ .<sup>33</sup> Finally, the samples were blow-dried by nitrogen (no rinsing with deionized water) and quickly transferred into the ALD system. A 60 nm thick thermal  $\text{Al}_2\text{O}_3$  layer was deposited at 200°C. The deposition rate was calibrated as 1.1 Å/cycle. The precursors were trimethylaluminum (TMAI) and water vapor ( $\text{H}_2\text{O}$ ). In a previous study,  $\text{Al}_2\text{O}_3$  layers were also used to passivate InP nanowires.<sup>34</sup> Scanning electron microscopy (SEM) images of InAsSb nanowires before and after  $\text{Al}_2\text{O}_3$  coating are shown in

Figure 1. It is clearly observed that the nanowires are conformally coated by the  $\text{Al}_2\text{O}_3$  layers, indicating that the deposition process is controllable.

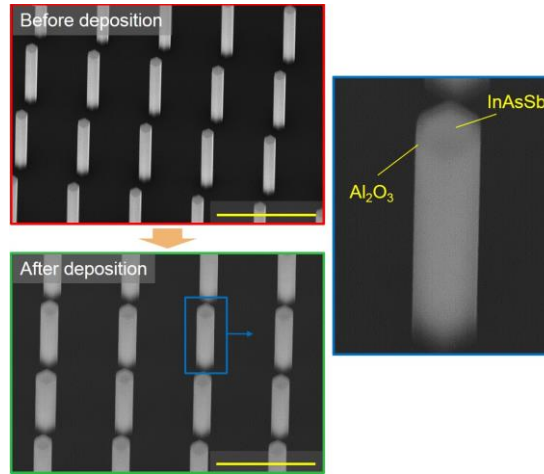


**Figure 1.** SEM images of InAsSb nanowires before and after a 60 nm  $\text{Al}_2\text{O}_3$  deposition. The scale bar is 2  $\mu\text{m}$ . The image on the right side shows a close-up look of a single nanowire conformally coated with  $\text{Al}_2\text{O}_3$  passivation layer.

Then, we performed PL characterizations to examine the quality of the surface passivation by comparing the intensities of PL emission from nanowire arrays with and without  $\text{Al}_2\text{O}_3$  layers. The measurement was carried out by a solid-state red laser at 671 nm and a liquid-nitrogen cooled InSb detector in a Thermo Scientific Nicolet 6700 Fourier-transform infrared (FTIR) spectrometer. For the PL measurement, we intentionally tested three nanowire arrays (samples A to C) with different nanowire dimensions, i.e., diameter ( $D_{\text{NW}}$ ) and height ( $H_{\text{NW}}$ ), which give different surface-to-volume ratios. Since the carrier motion in 3-D nanowire structures is complicated and closely correlated to their geometries, it is interesting to investigate the dependency of PL emission on nanowire dimensions and understand the comprehensive 3-D carrier dynamics. Figure 2 shows the SEM images of the nanowire array samples without  $\text{Al}_2\text{O}_3$  passivation from A to C and their low-temperature (77K) PL emission before and after the passivation process. No room-temperature PL emission was observed from the unpassivated InAsSb nanowires. It is clearly evident that the PL intensity in passivated nanowires is drastically enhanced by a factor of 10 to 50 times compared to unpassivated nanowires, which demonstrates the high quality of the surface passivation. Furthermore, it is noted that the  $\text{Al}_2\text{O}_3$  shells introduce compressive strains on the bulk

InAsSb nanowires, causing a blue-shift of PL emission peaks, which cannot be avoided in the passivation process. Interestingly, the enhancement of PL intensity is inversely correlated to the nanowire diameter. Sample B, which has the smallest nanowire diameter (151 nm), shows the most significant increase of PL emission (52-fold), while sample C, which has the largest nanowire diameter (220 nm), shows the least significant increase in PL emission (17-fold) after passivation. This is because the nonradiative recombination of the photogenerated carriers on surfaces is more significant in nanowires with smaller diameter, since the probability of those carriers diffusing to the surfaces are higher.

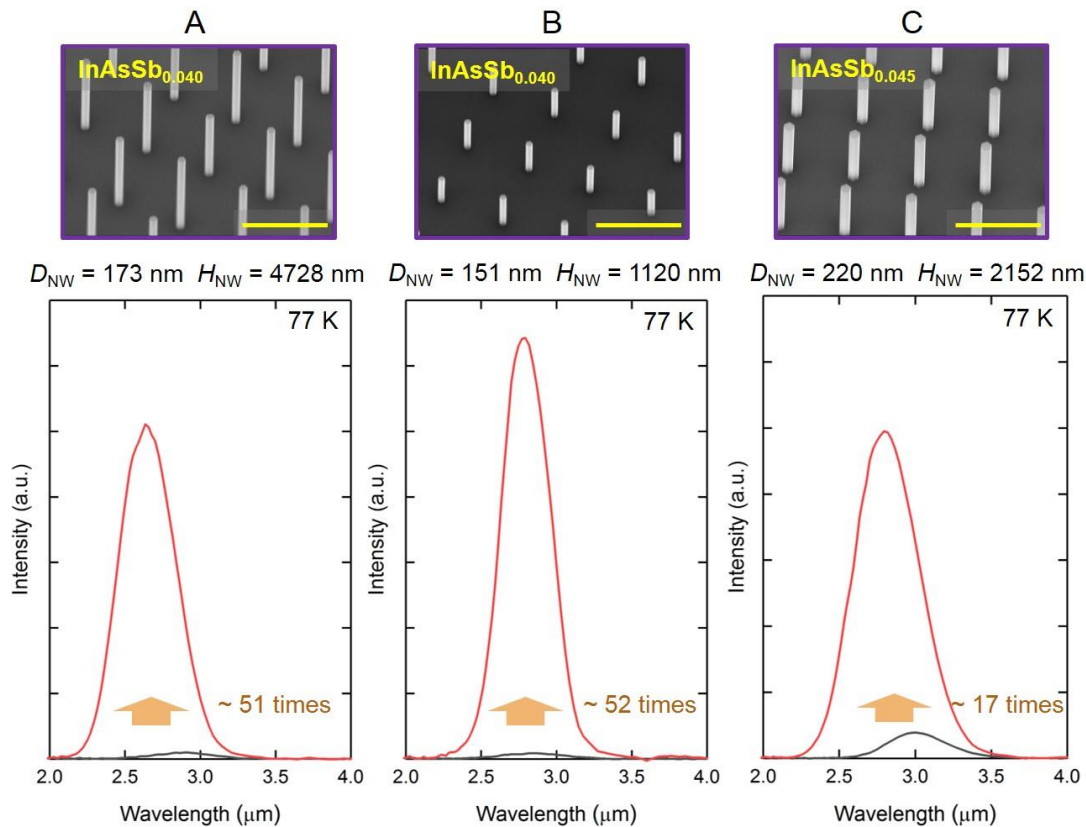


**Figure 2.** Samples A – C examine passivation quality of thin-film  $\text{Al}_2\text{O}_3$ . SEM images show the InAsSb nanowire dimensions before  $\text{Al}_2\text{O}_3$  deposition: (1) Sample A –  $D_{\text{NW}} = 173$  nm,  $H_{\text{NW}} = 4728$  nm; (2) Sample B –  $D_{\text{NW}} = 151$  nm,  $H_{\text{NW}} = 1120$  nm; (3) Sample C –  $D_{\text{NW}} = 220$  nm,  $H_{\text{NW}} = 2152$  nm; The scale bar is 2  $\mu\text{m}$ . The bottom PL-plots show a comparison of the low-temperature (77 K) PL emission of InAsSb nanowires with and without passivation layers. The enhancement ratios are labelled.

The correlation between the increase of PL emission to the improvement of surface recombination velocity (in units of cm/s) was further studied. Typically, the surface recombination velocity of nanowires is extracted by time-resolved photoluminescence (TRPL), as shown in many pioneering studies.<sup>28,29</sup> However, we believe that the rich information inherent in the PL spectra can still be harnessed to unveil the surface dynamics. The basic idea is as follows. We assumed the surface recombination velocity of unpassivated nanowires as  $v_s$  ( $1 \times 10^1 - 1 \times 10^6$  cm/s) and that of passivated nanowires as  $v_s'$  ( $1 \times 10^1 - 1 \times 10^6$  cm/s). We then applied a 3-D computational transient model to compute the radiative recombination over the nanowire segment at steady-state with constant light injection for each of the surface recombination velocity values. The enhancement of “PL” of nanowires with passivation layers, can be calculated as

$$R = I_2/I_1 \quad (1)$$

where  $R$  is the ratio or the factor of enhancement, and  $I_1$  and  $I_2$  are the simulated radiative recombination rates, or “PL intensities”, of the nanowires with and without the passivation layers, respectively. Here, we used a constant optical generation to represent the incoming continuous-wave (CW) laser. The radiative recombination coefficient of InAsSb at 77 K was set as  $1.2 \times 10^{-9}$  cm<sup>3</sup>·s<sup>-1</sup>. More detailed explanations of the transient modeling of PL are presented in the Supporting Information (Table S1).

Figure 3 shows the resultant simulations of the enhancement ratio  $R$  and its correlation with  $v_s$  and  $v_s'$ . The schematics of the simulated structures are shown in the upper-left corner of Figure 3a. Each point on the contour plot in Figures 3b-3d represents a certain combination of  $v_s$  and  $v_s'$ , i.e., the quality of unpassivated and passivated surface. The dashed contour line is a set of points which gives the same  $R$ . We can interpret the contour plots by observing sample B as an example (Figure 3c). All points, i.e., combinations of ( $v_s, v_s'$ ), on the contour line can give the same PL enhancement of 52. If  $v_s$  is between  $8 \times 10^4 - 1 \times 10^5$  cm/s, the corresponding  $v_s'$  is between  $1 \times 10^1 - 1 \times 10^3$  cm/s, meaning that the surface recombination velocity is suppressed by 100 – 8000 times with Al<sub>2</sub>O<sub>3</sub> passivation. Similarly, if  $v_s$  is between  $8 \times 10^5 - 1 \times 10^6$  cm/s, a possible range of  $v_s'$  is between  $2 \times 10^4 - 3 \times 10^4$  cm/s, suggesting a decrease of surface recombination velocity by a factor of 30 – 40 with Al<sub>2</sub>O<sub>3</sub> passivation. Although the exact value of  $v_s$  is

unknown, we can certainly gauge that it is between  $8 \times 10^4 - 1 \times 10^6$  cm/s. A surface recombination of  $(5.0 \pm 0.2) \times 10^4$  cm/s was previously reported for unpassivated InAs in InAs/GaSb type-II superlattices,<sup>35</sup> thus  $v_S$  of unpassivated InAs(Sb) nanowire can be estimated to be on the order of  $10^4$  cm/s. Thus, we conclude that for sample B,  $v_S$  must be between  $8 \times 10^4 - 1 \times 10^5$  cm/s, and  $v_S'$  is between  $1 \times 10^1 - 1 \times 10^3$  cm/s.

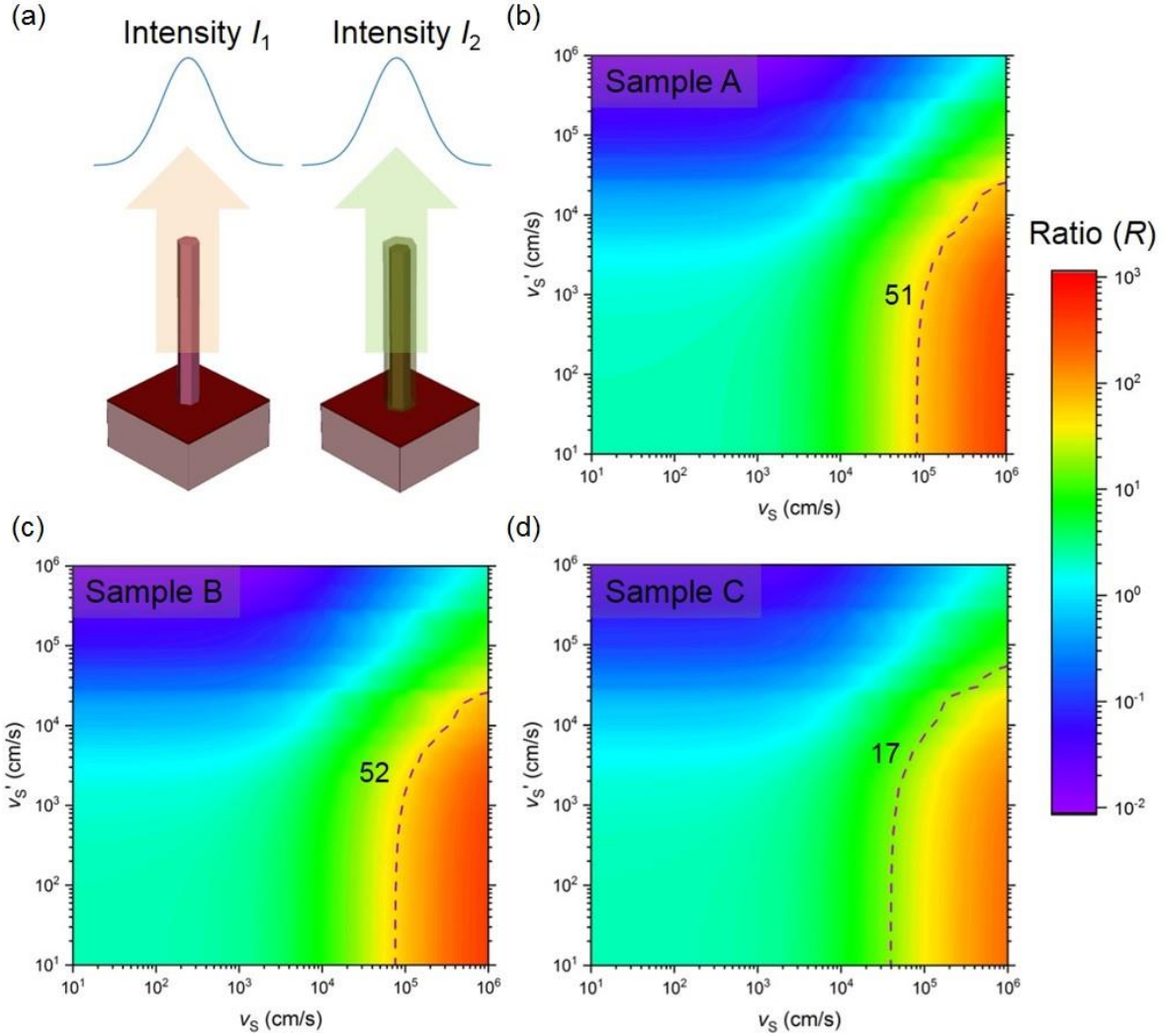


**Figure 3.** (a) Schematic diagram shows the structures of unpassivated and passivated nanowires used in the transient simulations. (b)-(d) Three contour plots show the simulated PL enhancement ratios corresponding to different combinations of  $(v_S, v_S')$ . The measured ratios ( $R$ ) are labelled along with the contour lines.

Next, we look at the other samples A and C (Figures 3b and 3d). The enhancement ratio  $R$  of sample A is 51, similar to that of sample B, as shown in Figure 3b. Their two contour lines almost overlap with

each other, and thus the actual values of  $v_s$  and  $v_s'$  of samples A and B are the same. As for sample C, the ratio  $R$  is 17, as shown in Figure 3d, much lower than those of samples A and B. Even so, we note that the intersections of the contour line with the  $x$ -axis ( $v_s$ ) and  $y$ -axis ( $v_s'$ ) for sample C is  $4 \times 10^4$  cm/s and  $5 \times 10^4$  cm/s, respectively, within the same orders as the other two cases (A and B). The smaller  $R$  results from a smaller surface-to-volume ratio of sample C due to its larger diameter. Consequently, the effect of surface recombination on the photogenerated carriers is not as sensitive as that for samples A and B. In other words, a smaller  $R$  does not necessarily mean that the surface quality is low. This is a unique property for nanowires, unlike planar thin-film devices, and hence require their 3-D geometries to be taken into account, and can only be fully understood when using a 3-D computational model. It is thus fair to assume that the surface quality of passivated nanowires of samples A – C is the same. If so,  $v_s$  of sample C is about  $4 \times 10^4$  –  $5 \times 10^4$  cm/s, which is slightly lower than that of samples A and B. Note that  $[x]_{sb}$  of Sample C is 0.045, slightly higher than that of samples A and B ( $[x]_{sb}$  was estimated based on the previous studies).<sup>20,23</sup> Thus, there might be a dependency of surface recombination velocity of unpassivated InAsSb nanowires on  $[x]_{sb}$ .

To examine the optical property of InAsSb nanowires at room temperature, we applied the same  $(\text{NH}_4)_2\text{S}/\text{Al}_2\text{O}_3$  passivation technique to InAsSb nanowires with different  $[x]_{sb}$  ranging from 0.02 to 0.18 (similarly,  $[x]_{sb}$  was estimated based on the previous studies).<sup>20,23</sup> Some of the nanowire samples were previously grown with nanowire pitch of 400 nm ( $[x]_{sb} > 0.07$ ).<sup>23</sup> The thickness of the  $\text{Al}_2\text{O}_3$  shell was kept fixed at 60 nm. Room-temperature PL emission from InAsSb nanowires spanning the entire MWIR regime is shown in Figure 4, which indicates high-quality of the surface passivation. This shows potential for achieving room-temperature photodetection at MWIR. The dips in the PL spectra of InAsSb nanowires with higher  $[x]_{sb}$  result from  $\text{CO}_2$  absorption, and the cutoff of the spectra at 5  $\mu\text{m}$  comes from the InSb detector. Note that since the PL emission peaks of passivated InAsSb nanowires show blue-shifts, they cannot be directly used to estimate  $[x]_{sb}$ .

**Fabrication process with  $\text{Al}_2\text{O}_3$  and uncooled photodetector.** After demonstrating the passivation technique, we developed a fabrication process for integrating  $\text{Al}_2\text{O}_3$  passivated nanowires with our standard nanowire device fabrication process. The goal was to only expose the top facets of nanowires while keeping

the sidewalls coated, which was done by selectively removing the  $\text{Al}_2\text{O}_3$  shells. This is because photogenerated carriers of nanowire photodetectors with self-aligned plasmonic gratings are tightly confined in the top nanowire segments, and well-passivated surfaces can reduce nonradiative recombination and enhance responsivity.<sup>9</sup> Unlike III-V semiconductor shells formed by *in-situ* passivation, e.g. In(Ga)(As)P and AlGaAs, the oxide-based shells show high selectivity to core materials, i.e., nanowires, in wet or dry etching. Another advantage of using oxide shells is that the top small bandgap materials for optical absorption are not depleted by the 3-D contacts, i.e., plasmonic gratings, which is commonly observed in previous nanowire-plasmonic photodetectors.<sup>9,17,30,31</sup>

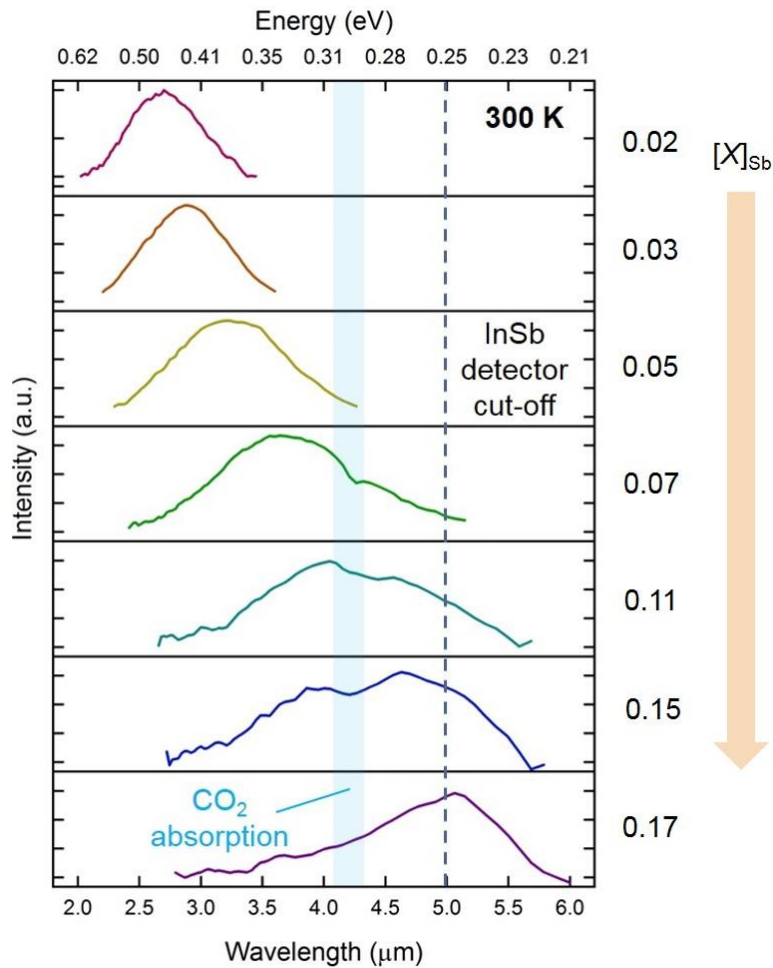


**Figure 4.** Room-temperature PL characterization of InAsSb nanowires passivated by  $(\text{NH}_4)_2\text{S}/\text{Al}_2\text{O}_3$ .  $[\text{x}]_{\text{sb}}$  ranges from 0.02 to 0.17. The composition was determined from the PL peaks of unpassivated InAsSb nanowires.

The schematic diagram of the fabrication process is shown in the top part of Figure 5(a). In this study, we tested two different strategies: (1) wet etching by buffered oxide etch (BOE), and (2) dry etching by reactive-ion etching (RIE) using  $\text{CHF}_3$  and Ar plasmas. We first performed the wet etching process and realized the process is not controllable (Supporting Information Figure S2). During the wet etching process, the BOE solution tended to penetrate between the BCB layer and  $\text{Al}_2\text{O}_3$  layer and etched the  $\text{Al}_2\text{O}_3$  underneath the exposed portion. As a result, gaps were created around the nanowire circumference, and became larger during the second etch-back process. This is undesirable since these gaps affect the quality of the tilted metal deposition. Note the second etch-back process is used to expose the adequate nanowire height, to achieve the desired plasmonic resonance absorption wavelength, prior to incorporating the plasmonic gratings. Thereafter, we examined the dry etching strategy, as shown in Figure 5(a). The dry etching was performed in an Oxford 80 Plus RIE system. The  $\text{CHF}_3$  and Ar flowrate was set to 25 sccm and 50 sccm respectively, while the pressure was 35 mTorr and power was 75 W. Remarkably, the nanowires were entirely capped by  $\text{Al}_2\text{O}_3$  shells while only the top facets were exposed, showing “pencil” shaped nanowire segments. The polymer by-products of  $\text{CHF}_3$ , i.e.,  $\text{C}_x\text{F}_y$ ,<sup>36</sup> coupled with BCB, immediately adjacent to the nanowire sidewalls, preserves the sidewall  $\text{Al}_2\text{O}_3$ , leading to anisotropic etching (Supporting Information Figure S3). The etching process was precisely controlled by using a very slow etch rate of 1.1 – 1.3 nm/min, with a total etching time of 45 – 55 minutes. The calibrated selectivity of  $\text{Al}_2\text{O}_3$  to BCB was between 1:4.2 and 1:4.5. No gaps between the nanowire and BCB along the nanowire circumference were observed before and after the  $\text{Al}_2\text{O}_3$  shell etching or the second etch-back.

To test whether the passivation was degraded after the entire dry etching process, we selected one InAsSb nanowire sample and fully removed the BCB layer after the shell etching. We then performed PL characterizations (77 K) on one nanowire array and compared its PL emission with the one measured right after the  $\text{Al}_2\text{O}_3$  deposition. All measurement conditions were kept fixed, and no degradation of PL signal was observed. Rather, the PL emission was even stronger, suggesting an enhanced light out-coupling efficiency due to the tapered nanowire tips with  $\text{Al}_2\text{O}_3$  shells. The details of this experiment are given in the Supporting Information Figure S4. Therefore, we conclude that the etching scheme displays excellent

compatibility with our standard nanowire device fabrication process and shows thermal stability at least up to 250°C (the temperature used for BCB curing). It is worth mentioning that no degradation of Al<sub>2</sub>O<sub>3</sub> has been found after one month (the PL spectra taken at different time periods overlapped), suggesting a reasonable long-term stability for device processing. A complete description of the fabrication process is given in the Supporting Information Figure S5.

Sample D (InAs<sub>0.955</sub>Sb<sub>0.045</sub>, nanowire pitch of 1300 nm), with  $D_{NW} = 264$  nm and  $H_{NW} = 1650$  nm, was fabricated using the aforementioned fabrication process. Other InAsSb samples with higher  $[x]_{Sb}$  (in Figure 4) were grown on patterns with nanowire pitch of 400 nm, which was not optimized to excite surface plasmon resonance at MWIR. Reflectance measurement on the fabricated device was performed using the FTIR spectrometer and an attached Thermo Scientific Nicolet Continuum microscope with a liquid-nitrogen cooled MCT-A detector. Figure 5(b) depicts the normalized absorbance plus transmittance, i.e. 1 - reflectance, from 1.5 to 5.0 μm under a broadband infrared source. The inset shows the top view of the fabricated nanowire-plasmonic array. Two peaks are observed at ~2.0 μm and ~3.5 μm, clearly indicating the surface plasmon resonance peaks excited by the 3-D plasmonic grating. This clearly indicates the absorption signatures at short-wavelength infrared (SWIR) and MWIR, which are achieved by using large nanowire pitch of 1300 nm and a large nanowire diameter over 200 nm.

Figure 5(c) shows a room-temperature spectral response at a reverse bias of 0.5 V from 1.5 to 5.0 μm. Note that the photocurrent spectrum is not normalized. Two detection peaks are clearly observed – one at ~2.0 μm and ~3.4 μm, corresponding to the absorption signatures in Figure 5(b). Due to the low  $v_s$  given by the Al<sub>2</sub>O<sub>3</sub> passivation, a portion of the photocarriers can be drifted to the 3-D contacts without recombining at nanowire surfaces. It should be noted that the spectral response in photovoltaic mode, i.e., 0 V, is too noisy to resolve. This is because, the InAsSb nanowires are unintentionally *n*-doped and the doping level is uniform, there is no additional electric field at nanowire tips where photogenerated carriers are located and thus, IQE is low at 0 V. Additionally, the detectivity ( $D^*$ ) of this device is expected to be low due to high leakage current at reverse bias (Supporting Information Figure S6, with more device characterizations). We suspect that the significant leakage results from the large InAsSb-SiO<sub>2</sub> interface

area, i.e., the excessive overgrowth on SiO<sub>2</sub> in the lateral direction. One potential solution is to selectively remove the SiO<sub>2</sub> growth mask after nanowire growth and passivate the entire nanowires and nanohole segments by Al<sub>2</sub>O<sub>3</sub> to reduce the nonradiative G-R process at InAsSb-SiO<sub>2</sub> interface. Note that this process requires a nanowire growth using nanoholes with larger diameter ( $\geq 80$  nm) to avoid “peeling-off” of nanowires due to hydrophobic effect during nanowire sulfuration.

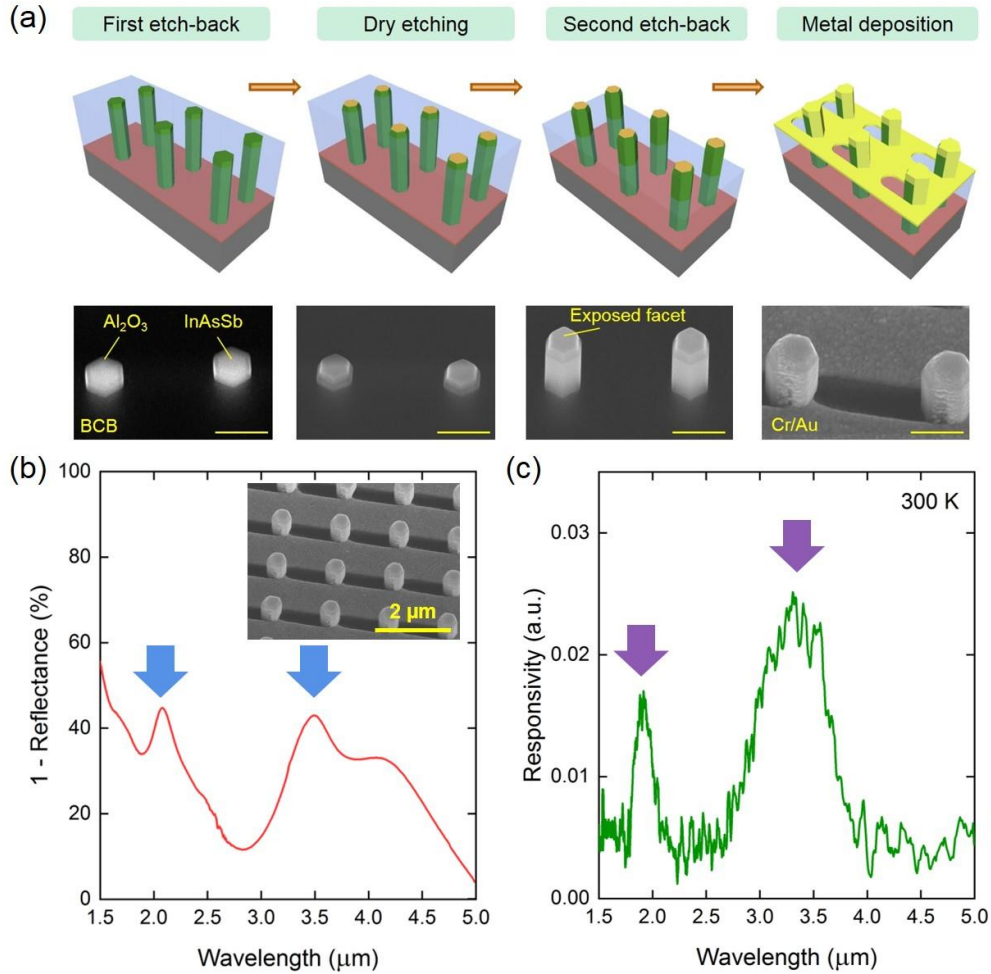


**Figure 5.** (a) Nanowire fabrication process with Al<sub>2</sub>O<sub>3</sub> passivation shells. Four major steps are shown. Dry etching process is carefully designed to expose only top nanowire facets with sidewalls entirely covered by the Al<sub>2</sub>O<sub>3</sub> layer. The scale bar is 500 nm. (b) Reflectance measurement. The y-axis is one minus reflectance, giving the sum of absorptance and transmittance. The inset shows the top view of the fabricated nanowire-plamonic array. (c) Spectral response measurement at room temperature (not normalized). The arrows highlight the peaks observed in both reflectance and spectral response measurement.

In this study, we demonstrated InAsSb nanowire photodetectors on InP substrate to approach room-temperature photodetection at MWIR. The photodetectors were comprised of nanostructured photoabsorbers,  $n$ -InAsSb/ $p$ -InP (nanowire-substrate)  $p$ - $n$  heterojunctions, and 3-D plasmonic gratings. We first developed an *ex-situ* passivation technique using  $(\text{NH}_4)_2\text{S}/\text{Al}_2\text{O}_3$  to reduce the nonradiative recombination at InAsSb nanowire surfaces. A significant suppression of surface recombination velocity was observed and PL emission from the InAsSb nanowires at room temperature was achieved, spanning the entire MWIR spectrum. Next, we developed a fabrication process based on dry etching to expose the nanowire top facets with sidewalls fully covered by the  $\text{Al}_2\text{O}_3$  shells. This process proved to be compatible with the standard fabrication process of vertical nanowires. Finally, we performed device characterizations on the fabricated InAsSb nanowire-plasmonic photodetectors and observed room-temperature photodetection at  $3.4 \mu\text{m}$ . The result matched the absorption signatures obtained by the reflectance measurement. Our work provides a foundation for achieving room-temperature (uncooled) operation of nanowire photodetectors for photodetection at MWIR or even longer wavelengths with significant applications in both industrial and research settings.

## **ASSOCIATED CONTENTS**

### **Supporting Information**

Growth calibration, transient modeling of photoluminescence, wet etching of Al<sub>2</sub>O<sub>3</sub> passivation shells, redeposition of CHF<sub>3</sub> by-products, reliability of dry etching process, complete fabrication process, more device characterizations. This material is available free of charge via the Internet at <http://pubs.acs.org>.

## **AUTHOR INFORMATION**

### **Corresponding Author**

\*Email: [dingkun.ren@ucla.edu](mailto:dingkun.ren@ucla.edu)

### **ORCID**

Dingkun Ren: 0000-0001-9470-1956

Alan C. Farrell: 0000-0001-6083-9121

Benjamin S. Williams: 0000-0002-6241-8336

### **Notes**

The authors claim no competing financial interest.

## **ACKNOWLEDGEMENTS**

We acknowledge the user facilities UCLA Nanoelectronics Research Facility (NRF) and Integrated Systems Nanofabrication Cleanroom (ISNC) in California NanoSystems Institute (CNSI). The authors would also like to thank ISNC staff members Tony Wright, Lorna Tokunaga, and Krissy Do for invaluable insight and support during this study. The authors also acknowledge the generous financial support of this research by National Science Foundation (grant no. ECCS-1509801), Air Force Office of Scientific Research (FA9550-15-1-0324), Sêr Cymru grants in Advanced Engineering and Materials, and Airbus Group Endeavr Wales.

## REFERENCES

(1) FLIR MWIR (InSb) FPA.

Available online: <https://www.flir.com/products/mwir-insb-fpa/>

(2) 640×512 Indium antimonide (InSb) MWIR infrared camera.

Available online: <http://www.ircameras.com/camera/irc906hs/>

(3) High speed MWIR camera extendable into the SWIR realm.

Available online: <http://www.xenics.com/en/camera/tigris-640/>

(4) Rogalski, A.; Martyniuk, P.; Kopytko, M. InAs/GaSb type-II superlattice infrared detectors: future prospect. *Appl. Phys. Rev.* **2017**, 4, (3), 031304.

(5) Rogalski, A.; Antoszewski, J.; Faraone, L. Third-generation infrared photodetector arrays. *J. Appl. Phys.* **2009**, 105, (9), 091101.

(6) Rogalski, A. Infrared detectors for the future. *Acta Phys. Pol. A* **2009**, 116, (3), 389-405.

(7) Martyniuk, P.; Antoszewski, J.; Martyniuk, M.; Faraone, L.; Rogalski, A. New concepts in infrared photodetector designs. *Appl. Phys. Rev.* **2014**, 1, (4), 041102.

(8) Ren, D.; Meng, X.; Rong, Z.; Cao, M.; Farrell, A. C.; Somasundaram S.; Azizur-Rahman, K. M.; Williams, B. S.; Huffaker, D. L. Uncooled photodetector at short-wavelength infrared using InAs nanowire photoabsorbers on InP with p-n heterojunctions (*under review, Nano Letters*)

(9) Ren, D.; Rong, Z.; Azizur-Rahman, K. M.; Somasundaram S.; Shahili, M.; Huffaker, D. L. Feasibility of achieving high detectivity at short- and mid-wavelength infrared using nanowire-plasmonic photodetectors with p-n heterojunctions (*in press, Nanotechnology*)

DOI: <https://doi.org/10.1088/1361-6528/aaed5c>

(10) Ren, D.; Farrell, A. C.; Williams, B. S.; Huffaker, D. L. Seeding layer assisted selective-area growth of As-rich InAsP nanowires on InP substrates. *Nanoscale* **2017**, 9 (24), 8220-8228.

(11) Du, W.-N.; Yang, X.-G.; Wang, X.-Y.; Pan, H.-Y.; Ji, H.-M.; Luo, S.; Yang, T.; Wang, Z.-G. The self-seeded growth of InAsSb nanowires on silicon by metal-organic vapor phase epitaxy. *J. Cryst. Growth* **2014**, 396, 33-37.

(12) Du, W.; Yang, X.; Pan, H.; Wang, X.; Ji, H.; Luo, S.; Ji, X.; Wang, Z.; Yang, T. Two different growth mechanisms for Au-free InAsSb nanowires growth on Si substrate. *Cryst. Growth Des.* **2015**, 15, (5), 2413-2418.

- (13) Du, W.; Yang, X.; Pan, H.; Ji, X.; Ji, H.; Luo, S.; Zhang, X.; Wang, Z.; Yang, T. Controlled-direction growth of planar InAsSb nanowires on Si substrates without foreign catalysts. *Nano Lett.* **2016**, 16, (2), 877-882.
- (14) Zhuang, Q. D.; Alradhi, H.; Jin, Z. M.; Chen, X. R.; Shao, J.; Chen, X.; Ana, M. S.; Cao, Y. C.; Liu, J. Y.; Yates, P.; Durose, K.; Jin, C. J. Optically efficient InAsSb nanowires for silicon-based mid-wavelength infrared optoelectronics. *Nanotechnology* **2017**, 28, (10), 105710.
- (15) Boland, J. L.; Amaduzzi, F.; Sterzl, S.; Potts, H.; Herz, L. M.; Fontcuberta i Morral, A.; Johnston, M. B. High electron mobility and insights into temperature-dependent scattering mechanisms in InAsSb nanowires. *Nano Lett.* **2018**, 18, (6), 3703-3710.
- (16) Xiaoguang, Y.; Wenna, D.; Xianghai, J.; Xingwang, Z.; Tao, Y. Defect-free InAsSb nanowire arrays on Si substrates grown by selective-area metal-organic chemical vapor deposition. *Nanotechnology* **2018**, 29, (40), 405601.
- (17) Lee, W.-J.; Senanayake, P.; Farrell, A. C.; Lin, A.; Hung, C.-H.; Huffaker, D. L. High quantum efficiency nanopillar photodiodes overcoming the diffraction limit of light. *Nano Lett.* **2016**, 16 (1), 199-204.
- (18) Thompson, M. D.; Alhodaib, A.; Craig, A. P.; Robson, A.; Aziz, A.; Krier, A.; Svensson, J.; Wernersson, L.-E.; Sanchez, A. M.; Marshall, A. R. J. Low leakage-current InAsSb nanowire photodetectors on silicon. *Nano Lett.* **2016**, 16 (1), 182-187.
- (19) Svensson, J.; Anttu, N.; Vainorius, N.; Borg, B. M.; Wernersson, L.-E. Diameter-dependent photocurrent in InAsSb nanowire infrared photodetectors. *Nano Lett.* **2013**, 13, (4), 1380-1385.
- (20) Farrell, A. C.; Lee, W.-J.; Senanayake, P.; Haddad, M. A.; Prikhodko, S. V.; Huffaker, D. L. High-quality InAsSb nanowires grown by catalyst-free selective-area metal-organic chemical vapor deposition. *Nano Lett.* **2015**, 15, (10), 6614-6619.
- (21) Zhuang, Q. D.; Anyebe, E. A.; Chen, R.; Liu, H.; Sanchez, A. M.; Rajpalke, M. K.; Veal, T. D.; Wang, Z. M.; Huang, Y. Z.; Sun, H. D. Sb-induced phase control of InAsSb nanowires grown by molecular beam epitaxy. *Nano Lett.* **2015**, 15, (2), 1109-1116.
- (22) Anyebe, E. A.; Rajpalke, M. K.; Veal, T. D.; Jin, C. J.; Wang, Z. M.; Zhuang, Q. D. Surfactant effect of antimony addition to the morphology of self-catalyzed InAs<sub>1-x</sub>Sb<sub>x</sub> nanowires. *Nano Res.* **2015**, 8, (4), 1309-1319.
- (23) Ren, D.; Farrell, A. C.; Huffaker, D. L. Selective-area InAsSb nanowires on InP for 3–5 μm mid-wavelength infrared optoelectronics. *MRS Advances* **2017**, 2 (58-59), 3565-3570.
- (24) Svensson, J.; Chen, Y.; Anttu, N.; Pistol, M.-E.; Wernersson, L.-E. Increased absorption in InAsSb nanowire clusters through coupled optical modes. *Appl. Phys. Lett.* **2017**, 110, (8), 081104.

- (25) Robson, M.; Azizur-Rahman, K. M.; Parent, D.; Wojdylo, P.; Thompson, D. A.; Lapierre, R. R. Multispectral absorbance from large-diameter InAsSb nanowire arrays in a single epitaxial growth on silicon. *Nano Futures* **2017**, 1, (3), 035001.
- (26) Ren, D.; Farrell, A. C.; Huffaker, D. L. Axial InAs (Sb) inserts in selective-area InAsP nanowires on InP for optoelectronics beyond 2.5  $\mu\text{m}$ . *Opt. Mater. Express* **2018**, 8 (4), 1075-1081.
- (27) Alhodaib, A.; Noori, Y. J.; Carrington, P. J.; Sanchez, A. M.; Thompson, M. D.; Young, R. J.; Krier, A.; Marshall, A. R. J. Room-temperature mid-infrared emission from faceted InAsSb multi quantum wells embedded in InAs nanowires. *Nano Lett.* **2018**, 18, (1), 235-240.
- (28) Ren, D.; Scofield, A. C.; Farrell, A. C.; Rong, Z.; Haddad, M. A.; Laghumavarapu, R. B.; Liang, B.; Huffaker, D. L. Exploring time-resolved photoluminescence for nanowires using a three-dimensional computational transient model. *Nanoscale* **2018**, 10 (16), 7792-7802.
- (29) Ren, D.; Rong, Z.; Somasundaram S.; Azizur-Rahman, K. M.; Liang, B.; Huffaker, D. L. A three-dimensional insight into correlation between carrier lifetime and surface recombination velocity for nanowires. *Nanotechnology* **2018**, 29 (50), 504003.
- (30) Senanayake, P.; Hung, C.-H.; Shapiro, J.; Lin, A.; Liang, B.; Williams, B. S.; Huffaker, D. L. Surface plasmon-enhanced nanopillar photodetectors. *Nano Lett.* 2011, 11, (12), 5279-5283.
- (31) Farrell, A. C.; Senanayake, P.; Meng, X.; Hsieh, N. Y.; Huffaker, D. L. Diode characteristics approaching bulk limits in GaAs nanowire array photodetectors. *Nano Lett.* **2017**, 17 (4), 2420-2425.
- (32) Ren, D.; Rong, Z.; Minh, C.; Farrell, A. C.; Meng, X.; Huffaker, D. L. Feasibility of room-temperature mid-wavelength infrared photodetectors using InAsSb nanostructured photoabsorbers. *Proc. SPIE* **2018**, 10531, 105310Y.
- (33) Higuera-Rodriguez, A.; Romeira, B.; Birindelli, S.; Black, L. E.; Smalbrugge, E.; van Veldhoven, P. J.; Kessels, W. M. M.; Smit, M. K.; Fiore, A. Ultralow surface recombination velocity in passivated InGaAs/InP nanopillars. *Nano Lett.* **2017**, 17, (4), 2627-2633.
- (34) Black, L. E.; Cavalli, A.; Verheijen, M. A.; Haverkort, J. E. M.; Bakkers, E. P. A. M.; Kessels, W. M. M. Effective surface passivation of InP nanowires by atomic-layer-deposited  $\text{Al}_2\text{O}_3$  with  $\text{PO}_x$  interlayer. *Nano Lett.* **2017**, 17, (10), 6287-6294.
- (35) Li, J. V.; Chuang, S. L.; Aifer, E.; Jackson, E. M. Surface recombination velocity reduction in type-II InAs/GaSb superlattice photodiodes due to ammonium sulfide passivation. *Appl. Phys. Lett.* **2007**, 90, (22), 223503.
- (36) Henri, J.; Han, G.; Meint de, B.; Miko, E.; Jan, F. A survey on the reactive ion etching of silicon in microtechnology. *J. Micromechanics Microengineering* **1996**, 6, (1), 14.